Numerical Simulation of Fluid Flow and Heat Transfer in a Curved Square Duct by using the Lattice Boltzmann Method

Quan Liao & T. C. Jen

Published online: 30 Jul 2008.

Submit your article to this journal

Article views: 115

View related articles

Citing articles: 5 View citing articles

NUMERICAL SIMULATION OF FLUID FLOW AND HEAT TRANSFER IN A CURVED SQUARE DUCT BY USING THE LATTICE BOLTZMANN METHOD

Quan Liao[1] and T. C. Jen[2]

[1]College of Power Engineering, Chongqing University, Chongqing, People's Republic of China
[2]Department of Mechanical Engineering, University of Wisconsin—Milwaukee, Milwaukee, Wisconsin, USA

In this article, the three-dimensional 27-velocities (D3Q27) lattice Boltzmann method (LBM) is employed to simulate the fully developed fluid flow and heat transfer in a curved square duct with curvature ratio 0.05–1.0 and Dean number 0–200. The so-called Dean instability in the curved square duct is fully investigated. It is found that for the square duct with high curvature ratio, the onset of transition from single-pair vortex to double-pair vortex depends on both Dean number and curvature ratio. This is consistent with conventional computational fluid dynamic (CFD) and experimental results, and the differences between simulation and experiment are very small. For the friction coefficient and Nusselt number, which are functions of Dean number and curvature ratio, it is found that the numerical results are in good agreement not only with the available experimental correlation but also with conventional CFD results under the given conditions.

INTRODUCTION

The study of viscous flow in curved ducts is of fundamental interest in fluid mechanics due to the numerous applications such as flows through turbomachinery blade passages, aircraft intakes, diffusers, heat exchangers, and so on [1–6]. The major effect of curved ducts on the fluid flow involves the strong secondary flow due to the longitudinal curvature in the geometry [7–9]. The presence of longitudinal curvature generates centrifugal force (which is perpendicular to the main flow along the axis) and produces so-called secondary flow on the cross sections of ducts. As a consequence of this centrifugal force, the axial velocity profile is distorted (from the typical parabolic velocity profile in straight ducts), with an outward shift of the peak axial velocity, and the total flow rate is reduced due to the decrease of average axial velocity.

NOMENCLATURE

A	cross-sectional area of square duct	P	wetted perimeter of square duct
c	lattice speed	Pr	Prandtl number
c_s	speed of sound	R	radius of curved duct
C	curvature ratio	Re	Reynolds number
C_f	Fanning friction factor	t	time variable
D_h	equivalent hydrodynamic diameter of square duct	T_m	mean temperature
		T_w	wall temperature
Dn	Dean number	T^*	dimensionless temperature
$\vec{e}_\alpha$	discrete particle velocity	$\vec{u}$	macroscopic velocity
f	mass density distribution function	U	average axial velocity
$f^{(eq)}$	local equilibrium distribution function	$\vec{x}$	space variable
		α	thermal diffusivity
$\bar{f}_\alpha$	post collision state of distribution function	δt	time step
		δx	lattice constant
f_c	friction factor for curved duct	λ	relaxation time
f_s	friction factor for straight duct	υ	kinetic viscosity
$\bar{h}$	average heat transfer coefficient	ρ	mass density
L	side length of square duct	$\vec{\xi}$	microscopic particle velocity
M	Mach number	τ	dimensionless relaxation time
Nu	Nusselt number	τ_T	heat transfer relaxation time
p	pressure	τ_w	Average wall shear stress
p_α	pressure distribution function	ω_α	weight factor

In the past two decades, the lattice Boltzman method (LBM) has been successfully applied to simulate all kinds of hydrodynamic fluid flows with complex boundary geometries [10, 11]. Compared with the conventional computational fluid dynamics (CFD) methods (which are based on continuum theory with macroscopic scale), the LBM is based on microscopic level and mesoscopic kinetic equations, in which the collective behavior of particles is used to simulate the continuum properties in a system. From the mathematical point of view, the LBM is a special finite-difference discretization of the Boltzmann equation with Bhatnagar-Gross-Krook (BGK) approximation. Due to its simple implementation (i.e., streaming and collision), easy grid generation, and powerful complex-geometry treatment ability, the LBM has been widely used in many research areas, such as multiple phases flow, fluid flow in porous media, and so on [12–16].

To the authors' best knowledge, the LBM has never been used to solve the fluid flow and heat transfer problems in a curved square duct in which the flow pattern is much more complicated than that in a straight duct. Therefore, it is proposed in this article to use a three-dimensional 27-velocities (D3Q27, as shown in Figure 1) incompressible LBM model [17, 18] and a passive-scalar thermal method to solve the fully developed fluid flow and heat transfer in a curved square duct. The flow pattern transition, friction coefficient, and Nusselt number are thoroughly investigated, and the comparisons show good agreement between the results of conventional CFD methods (i.e., Fluent software) or experimental correlations and those of LBM solutions. In addition, it is also shown that this method can be more easily implemented than the conventional CFD methods.
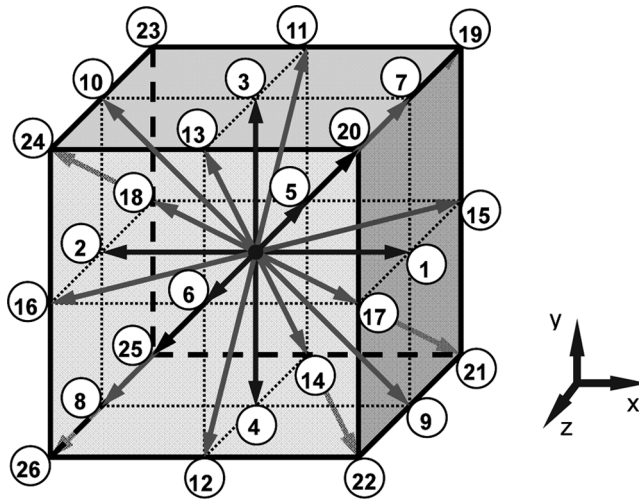
Figure 1. D3Q27 lattice model.

THE LATTICE BOLTZMANN METHOD

It is well known that conventional CFD methods compute the pertinent fields, such as velocity $\vec{u}$ and pressure p, by solving the Navier-Stokes equations numerically in space ($\vec{x}$) and time (t). However, the kinetic methods use the transport equation, such as the Boltzmann equation in particular, to solve the problems in a fluid dynamics field [19].

The lattice Boltzmann equation approximates the kinetic equation for a single particle mass density distribution $f(\vec{x}, \vec{\xi}, t)$ on the mesoscopic level. For example, the Boltzmann equation with the single time relaxation approximation (i.e., the BGK approximation) is

$$\frac{\partial f}{\partial t} + \xi \bullet \nabla f = -\frac{1}{\lambda}(f - f^{(eq)}) \tag{1}$$

where $\vec{\xi}$ is microscopic particle velocity, $f^{(eq)}$ is local equilibrium distribution (or Maxwell Boltzmann distribution), which has exactly the same mass density and macroscopic velocities of a gas as given by the distribution f at specific location, and λ is the so-called relaxation time.

In Eq. (1), the right-hand-side term models the effect of the fluid viscosity on the molecular level through the collision (or relaxation) process. The macroscopic quantities (such as mass density ρ and velocity $\vec{u}$) are the hydrodynamic first and second moments of the distribution f,

$$\rho = \int f(\vec{x}, \vec{\xi}, t) \, d^3\vec{\xi} \tag{2}$$

$$\rho \cdot \vec{u} = \int \vec{\xi} \cdot f(\vec{x}, \vec{\xi}, t) \, d^3\vec{\xi} \tag{3}$$

Since the theoretical premises of the lattice Boltzmann equation (LBE) are that (1) hydrodynamics is insensitive to the details of microscopic physics, and

(2) hydrodynamics can be preserved as long as the conservation laws and associated symmetries are satisfied at the microscopic level, the velocity space $\vec{\xi}$ can be discretized into a very small, finite set of velocities $\{\vec{\xi}_\alpha\}$ without seriously degrading the hydrodynamics. Therefore, in the finite discretized velocity space, the Boltzmann equation becomes,

$$\frac{\partial f_\alpha}{\partial t} + \vec{\xi}_\alpha \bullet \nabla f_\alpha = -\frac{1}{\lambda}(f_\alpha - f_\alpha^{(eq)}) \tag{4}$$

with the distribution function of discrete velocities $f_\alpha(\vec{x}, t) \equiv f(\vec{x}, \vec{\xi}_\alpha, t)$. The local equilibrium distribution $f_\alpha^{(eq)}$ and the discrete velocity set $\{\vec{\xi}_\alpha\}$ for the D3Q27 LBE model are

$$f_\alpha^{(eq)} = \omega_\alpha \rho \left[1 + \frac{3 \cdot (\vec{e}_\alpha \bullet \vec{u})}{c^2} + \frac{9 \cdot (\vec{e}_\alpha \bullet \vec{u})^2}{2 \cdot c^4} - \frac{3 \cdot (\vec{u} \bullet \vec{u})}{2 \cdot c^2} \right] \tag{5}$$

where $\vec{e}_\alpha$ is the discrete particle velocity, $c = \delta x / \delta t$ is the lattice speed, $\vec{u}$ is the macroscopic velocity, ω_α is the weight factors, and δx and δt are the lattice constant and time step, respectively.

$$e_\alpha = \begin{cases} (0,0,0) & \alpha = 0 \\ (\pm 1, 0, 0)c, \ (0, \pm 1, 0)c, \ (0, 0 \pm 1)c & \alpha = 1, 2, \ldots, 6 \\ (\pm 1, \pm 1, 0)c, \ (0, \pm 1, \pm 1)c, \ (\pm 1, 0, \pm 1)c & \alpha = 7, 8, \ldots, 18 \\ (\pm 1, \pm 1, \pm 1)c & \alpha = 19, 20, \ldots, 26 \end{cases} \tag{6}$$

$$\omega_\alpha = \begin{cases} 8/27 & \alpha = 0, \\ 2/27 & \alpha = 1, 2, \ldots, 6 \\ 1/54 & \alpha = 7, 8, \ldots, 18 \\ 1/216 & \alpha = 19, 20, \ldots, 26 \end{cases} \tag{7}$$

With the velocity space discretized, the hydrodynamic moments are evaluated by

$$\rho = \sum_\alpha f_\alpha = \sum_\alpha f_\alpha^{(eq)} \tag{8}$$

$$\rho \cdot \vec{u} = \sum_\alpha \vec{e}_\alpha \cdot f_\alpha = \sum_\alpha \vec{e}_\alpha \cdot f_\alpha^{(eq)} \tag{9}$$

Discretizing Eq. (4) in space $\vec{x}$ and time t and rearranging, one obtains the following discretized lattice Boltzmann equation:

$$f_\alpha(\vec{x}_i + \vec{e}_\alpha \cdot \delta t, t + \delta t) - f_\alpha(\vec{x}_i, t) = -\frac{1}{\tau}[f_\alpha(\vec{x}_i, t) - f_\alpha^{(eq)}(\vec{x}_i, t)] \tag{10}$$

where $\tau = \lambda / \delta t$ is the dimensionless relaxation time.

Equation (10) is the so-called lattice Boltzmann equation with BGK approximation, and it is often referred as the LBGK model. By using a lengthy and complicated multiscale technique (i.e., Chapman-Enskog expansion) on the Boltzmann BGK equation [i.e., Eq. (1)], the conventional Navier-Stokes equation can be recovered, and the corresponding pressure and kinetic viscosity for the fluid

are defined as follows:

$$p = \frac{\rho \cdot k_B T}{m} \tag{11}$$

$$\upsilon = \frac{c^2 \cdot (\tau - 0.5) \cdot \delta t}{3} \tag{12}$$

Since the equilibrium distribution [Eq. (5)] has implicit nature in time and the LBGK model [Eq. (10)] has a Lagrangian nature in space discretization, the LBGK model is a second-order method in space and time for compressible fluid flow, and it can be solved by the following two consecutive steps:

Collision step:

$$\bar{f}_\alpha(\vec{x}_i, t) = f_\alpha(\vec{x}_i, t) - \frac{1}{\tau} [f_\alpha(\vec{x}_i, t) - f_\alpha^{(\text{eq})}(\vec{x}_i, t)] \tag{13}$$

Streaming step:

$$f_\alpha(\vec{x}_i + \vec{e}_\alpha \cdot \delta t, t + \delta t) = \bar{f}_\alpha(\vec{x}_i, t) \tag{14}$$

where $\bar{f}_\alpha$ denotes the postcollision state of the distribution function. It is apparent that the collision step is completely local (which is the native parallel computing feature of LBM without any other efforts as compared to the conventional CFD method), and the streaming step is easy to implement and requires little computational effort.

It is worth noting that the above mass density representative LBGK scheme is a kind of compressible fluid model, i.e., the mass density is one of the primitive variables. In the real world, all the fluids are theoretically compressible; therefore the mass density is always a function of space and time. However, for lower-speed fluid flow problems (in which the Mach number is very close to zero), the incompressible fluid assumption is widely used in real applications because of the simple governing equations and acceptable errors. For the condition of low Mach number, the fluctuation of mass density is small enough to neglect, and then the pressure can be used as an independent variable to replace the mass density. Therefore, the incompressible LBE model can be obtained within this incompressible fluid flow limit.

For a compressible fluid within an incompressible limit, it is well understood that the mass density is approximately a constant, ρ_0, and the density fluctuation, $\delta\rho$, should be of the order $O(M^2)$ in the limit of $M \to 0$, where M is the Mach number. If one explicitly plugs $\rho = \rho_0 + \delta\rho$ into the equilibrium distribution function, $f_\alpha^{(\text{eq})}$, and neglects the terms that are proportional to $\delta\rho(u/c)$ and $\delta\rho(u/c)^2$ [which are of the order $O(M^3)$ or higher], then the equilibrium distribution function becomes

$$f_\alpha^{(\text{eq})} = \omega_\alpha \left\{ \rho + \rho_0 \left[\frac{3 \cdot (e_\alpha \bullet u)}{c^2} + \frac{9 \cdot (e_\alpha \bullet u)^2}{2 \cdot c^4} - \frac{3 \cdot (u \bullet u)}{2 \cdot c^2} \right] \right\} \tag{15}$$

If a local pressure distribution function, $p_\alpha \equiv c_s^2 f_\alpha$, is introduced into the above equilibrium equation, then the pressure representative "incompressible" equilibrium

equation can be evaluated as

$$p_\alpha^{(eq)} = c_s^2 f_\alpha^{(eq)} = \omega_\alpha \left\{ p + p_0 \left[\frac{3 \cdot (e_\alpha \bullet u)}{c^2} + \frac{9 \cdot (e_\alpha \bullet u)^2}{2 \cdot c^4} - \frac{3 \cdot (u \bullet u)}{2 \cdot c^2} \right] \right\} \quad (16)$$

where c_s is the speed of sound, and $c_s = c/\sqrt{3}$ for the D3Q27 model. Then the corresponding evolution equation of the LBE system for incompressible fluid flow becomes

$$p_\alpha(\vec{x}_i + \vec{e}_\alpha \cdot \delta t, t + \delta t) - p_\alpha(\vec{x}_i, t) = -\frac{1}{\tau} [p_\alpha(\vec{x}_i, t) - p_\alpha^{(eq)}(\vec{x}_i, t)] \quad (17)$$

The pressure p and the macroscopic velocity $\vec{u}$ are evaluated by

$$p = \sum_\alpha p_\alpha \quad (18)$$

$$p_0 \cdot \vec{u} = \sum_\alpha \vec{e}_\alpha \cdot p_\alpha \quad (19)$$

The pressure representative incompressible LBE system can be solved by the same procedure, i.e., collision and streaming, as the mass density representative compressible LBE in Eqs. (13) and (14). In this article, the fully developed fluid flow in a curved square duct is solved by this method. Since this incompressible LBE model is based on the incompressible limit for compressible fluid, the Mach number has to be much smaller than unity (the Mach number usually cannot be greater than 0.15 in this incompressible fluid limit) if the simulation results are to be acceptable.

PASSIVE SCALAR METHOD FOR THE THERMAL LATTICE BOLTZMANN MODEL

The passive scalar approach [20, 21] utilizes the fact that, compared to the fluid flow LBE model, the macroscopic temperature satisfies a much simpler passive scalar equation (which can be simulated by solving an additional LBE) if the viscous dissipation and compression work done by the pressure are negligible. Therefore, in the passive-scalar thermal LBE model, the temperature is simulated using a separate distribution function which is independent of the fluid mass density or pressure distribution. However, this independent distribution function has the same lattice velocity (i.e., D3Q27 in this article) and equilibrium distribution function as fluid flow; this is different from the double-population method or multispeed LBE thermal model [22] (which have their own lattice velocity and equilibrium distribution function).

Similar to the kinetic viscosity in fluid flow LBE model, the corresponding thermal diffusivity in the passive scalar model is defined as

$$\alpha = \frac{c^2}{3} \left(\tau_T - \frac{1}{2} \right) \Delta t \quad (20)$$

where τ_T is the corresponding heat transfer relaxation time.

Since the viscosity in the LBE model is defined as

$$\upsilon = \frac{c^2}{3}\left(\tau_\upsilon - \frac{1}{2}\right)\Delta t \tag{21}$$

The corresponding Prandtl number of the fluid is

$$\Pr = \frac{\upsilon}{\alpha} = \frac{2\tau_\upsilon - 1}{2\tau_T - 1} \tag{22}$$

Although there are some apparent shortcomings to the passive-scalar thermal lattice Boltzmann model (for example, the viscous dissipation and compressible work done by pressure cannot be taken into account), the main advantage of this method is the enhancement of numerical stability compared to the multispeed thermal lattice Boltzmann models. It has been shown that this passive scalar method has the same stability as the fluid flow LBE model [20, 21]. In this article, this thermal method is adopted to solve the fully developed heat transfer in a curved square duct.

PHYSICAL MODEL DESCRIPTION

As shown in Figure 2, a curved square duct with side length L is placed on the horizontal plane, and the radius of the curved duct is R, measured from the center of duct to the center of the curve. The fluid flows in the square duct about the center of curvature toward the inside of the plane of the paper.

The curvature ratio of this curved duct is defined as

$$C = \frac{D_h}{R} \tag{23}$$

where D_h is the equivalent hydrodynamic diameter of the square duct, which is defined as

$$D_h = \frac{4A}{P} = \frac{4L^2}{4L} = L \tag{24}$$
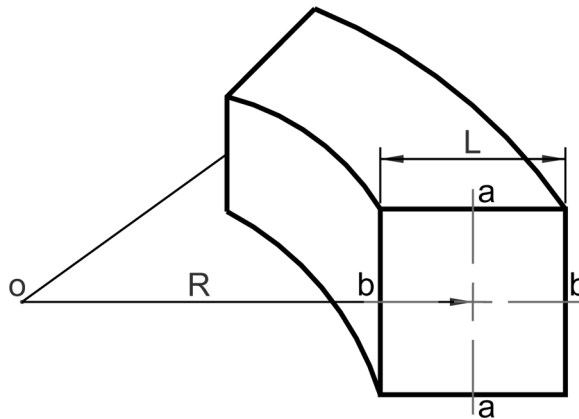
Figure 2. Geometry of curved square duct.

The nondimensional characteristic Dean number Dn is defined as a function of Reynolds number and curvature ratio:

$$Dn = Re \cdot (C)^{0.5} \tag{25}$$

$$Re = \frac{U \cdot D_h}{\upsilon} \tag{26}$$

where Re is the Reynolds number of the duct flow. A uniform grid is used in this article, and the corresponding relaxation factors for fluid flow and heat transfer are in the range 0.6–1.0.

On each cross section of the curved duct, a constant pressure gradient is introduced to drive fluid flow along the duct's axial direction. Due to the longitudinal curvature and axial velocity, the centrifugal force is involved and drives the fluid flow far away from the center of the curved duct (i.e., point O as shown in Figure 2), and then the so-called secondary flow is formed on the cross section. In this article, both pressure gradient and centrifugal force are treated like body forces acting on each interior lattice with different directions on the cross section of the duct (which is the projection of the computational domain), and the macroscopic momentum conservation method [23, 24] is used to apply these body forces to the LBE fluid flow and heat transfer models.

MATHEMATIC MODEL AND BOUNDARY CONDITIONS

Mathematic Model

In Figure 2, the fluid flows in the square duct point toward the inside of the plane of the paper. Since the fully developed fluid flow and heat transfer will be studied numerically in this article, the axial velocity profile and dimensionless temperature distribution on the cross section will not be changed along the main flow direction. Therefore, the original computation domain, which consists of the square cross section and curved duct, can be simplified to a domain including the square cross section and a few lattice lengths perpendicular to this section plane. As a result of this simplification, the basic LBM with uniform lattice can be used to solve this problem without any special treatment for the curved boundary. It is worth noting that although the original computation domain has been simplified, the fluid flow and heat transfer simulations are still in three dimensions, i.e., two dimensions on the cross section and one dimension in the axial flow direction.

For fluid flow in pipes, the Fanning friction factor is defined as [25]

$$C_f = \frac{2 \cdot \tau_w}{\rho \cdot V_{avg.}^2} \tag{27}$$

where τ_w is the average wall shear stress and is defined as

$$\tau_w = \mu \cdot \overline{\frac{dU_z}{dn}} \tag{28}$$

Plugging Eq. (28) and Eq. (26) into Eq. (27) and rearranging, one obtains the following friction factor for the curved duct:

$$C_f \cdot \mathrm{Re} = \frac{2 \cdot D_h}{V_{\mathrm{avg.}}} \cdot \overline{\frac{dU_z}{dn}} \tag{29}$$

As far as fluid flow in straight square duct is concerned, the analytical friction factor is available in literature and equals 14.25 [26].

For heat transfer in the curved duct, the corresponding dimensionless temperature and Nusselt number are defined as follows:

$$T^* = \frac{T_w - T}{T_w - T_m} \tag{30}$$

$$\mathrm{Nu} = \frac{\bar{h} \cdot D_h}{k} \tag{31}$$

where T_w and T_m are the wall temperature and mean temperature across the duct, respectively. $\bar{h}$ is the average heat transfer coefficient around the four wall sides and is defined as

$$\bar{h} = \frac{-k \cdot \overline{\partial T}/\partial n}{T_w - T_m} \tag{32}$$

Plugging Eq. (30) and Eq. (32) into Eq. (31) and rearranging, one obtains:

$$\mathrm{Nu} = D_h \cdot \overline{\frac{\partial T^*}{\partial n}} \tag{33}$$

For the fluid flow and heat transfer in a straight square duct, the analytical Nusselt number with constant wall temperature is 2.98 [26].

In order to obtain more accurate results, the two-dimensional Simpson integration method is used to calculate the average axial velocity based on the uniform lattice on the cross section.

Boundary Conditions

In the simplified computation domain, the boundary conditions have to be specified in two parts with three directions, i.e., axial flow direction and two directions on the cross-section plane.

Axial flow direction. Since both the fluid flow and heat transfer are fully developed, the velocity and dimensionless temperature profiles will not change along the axial flow direction (which is perpendicular to the plane of the paper and toward inside). Therefore, a simple periodic boundary can be naturally applied for both fluid flow and heat transfer in this direction, without any special treatment for the curved boundary.

Cross-section plane. On the duct cross section, four sides of wall are needed to specify the boundary conditions. In this mathematic model, the no-slip boundary and constant wall temperature conditions are applied on the four duct walls for fluid flow and heat transfer, respectively. The second-order-extrapolation boundary treatment [27] and counter-slip thermal boundary treatment [28] are employed for the fluid flow and heat transfer to determine the unknown distributions (i.e., pressure and dimensionless temperature distributions) coming from outside the computation domain.

Once all these boundary conditions are established, the fully developed fluid flow and heat transfer in the straight square duct are simulated using the current LBM model by letting curvature ratio approach to zero (i.e., the radius of the curved duct, R, is big enough, for example, 10^9), and the convergence criterion in this test simulation is that the relative error of total velocity (including three components) on each uniform lattice is less than 1.0×10^{-4} for every 400 consecutive time steps. After the convergence criterion is reached, the simulation results show that both friction coefficient and Nusselt number are in very good agreement with analytical results (i.e., the relative errors versus analytical results are less than 0.1%). This validates that this LBM model is correct and that the simplification of the computation domain is feasible and applicable. In addition to this benchmark validation of the straight duct, a grid convergence test was implemented before any data were adopted. For a given fluid flow problem, different numbers of uniform lattices (i.e., $50 \times 50 \times 3$, $100 \times 100 \times 3$, and $160 \times 160 \times 3$, where three lattices are used for the periodic direction) for the same computation domain were used to compare the differences in terms of friction coefficient and flow pattern on the cross section. After a couple of comparisons, it was found that the uniform lattice $100 \times 100 \times 3$ has both good accuracy and less computing cost. Therefore, the $100 \times 100 \times 3$ uniform lattice mesh is used in this article to simulate the fluid flow and heat transfer problems.

SIMULATION RESULTS AND DISCUSSION

Fluid Flow

As shown in Figure 3, the nondimensional axial velocity distribution of cross section b–b is presented at different Dean numbers with a constant curvature ratio $C = 0.05$. From this figure, it is evident that, as the Dean number increases, the maximum axial velocity first shifts toward the outside of the duct from near the center position until it reaches a most outside point on the cross section; then, once the Dean number reaches a certain value (which is a function of the curvature ratio), the velocity profile on cross section b–b suddenly changes to a new pattern (as shown in Figure 3), and the location of maximum axial velocity is much closer to the center of the duct than before. Moreover, as the Dean number increases further, the maximum axial velocity moves toward the center of the duct, which is the opposite moving direction compared to the case with smaller Dean number before the new velocity profile was observed.

With the same conditions, the dimensionless axial velocity profile along cross section a–a is shown in Figure 4. In this figure, it is apparent that as the
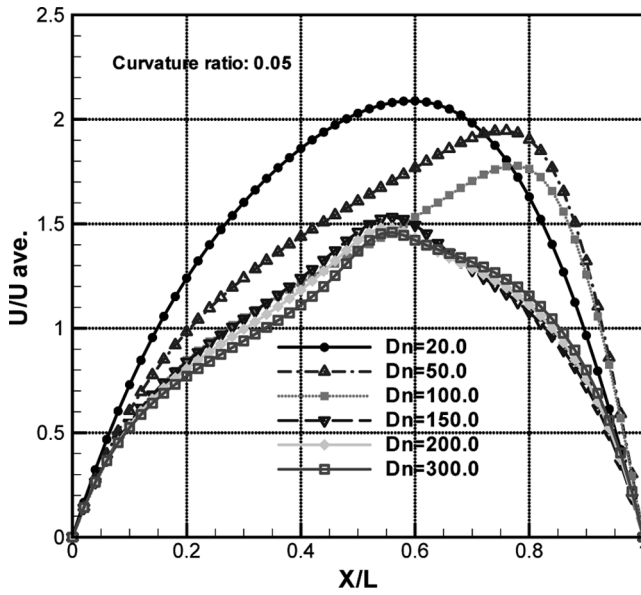
Figure 3. Velocity distributions along cross section *b–b*.

Dean number increases, the peak of the velocity profile on cross section *a–a* changes from one point at the beginning to two symmetrical points, and eventually up to three points (one is at the center and the other two are symmetrical about
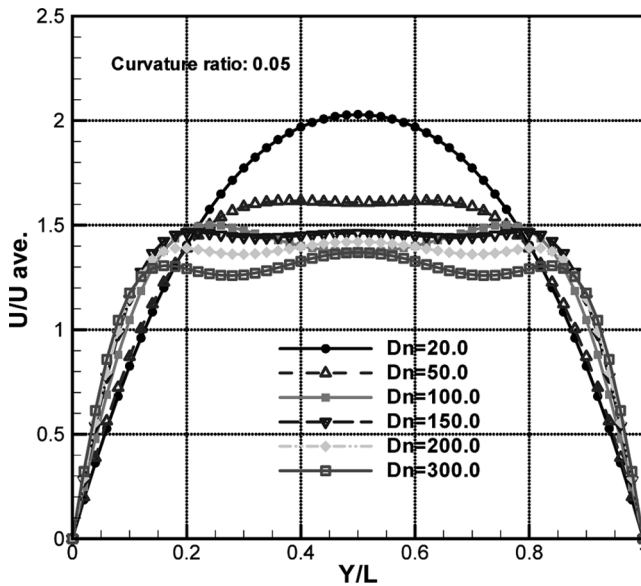
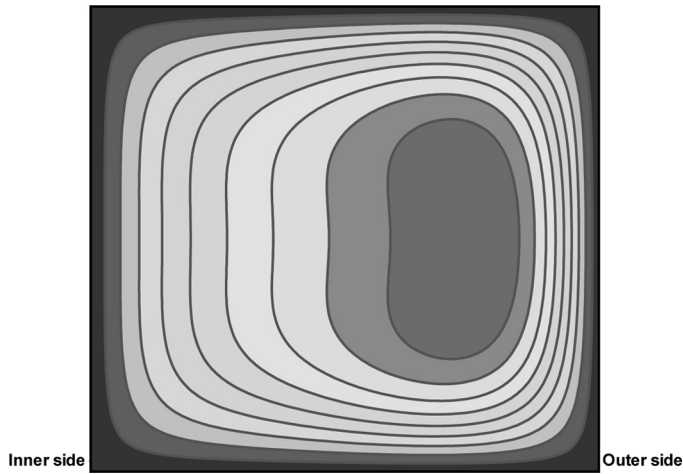**Figure 4.** Velocity distributions along cross section *a–a*.

Figure 5. Velocity contour of cross section (Dn = 50.0, C = 0.05).

the center one). Meanwhile, the axial velocity on cross section *a–a* is becoming more uniform as Dean number increases. The switchback movement of maximum axial velocity on cross section *b–b* in Figure 3 and the change of number of peak velocities on plane *a–a* in Figure 4 can be explained as follows. On the duct cross section, the centrifugal force (which is induced by axial velocity and duct curvature) drives the fluid flow from inner side wall to the outer side wall, and this fluid flow causes a symmetrical flow pattern on the cross section for the horizontal curved duct. Compared to the main axial fluid flow (which is perpendicular to cross section), the flow on the cross section is called secondary flow. When the
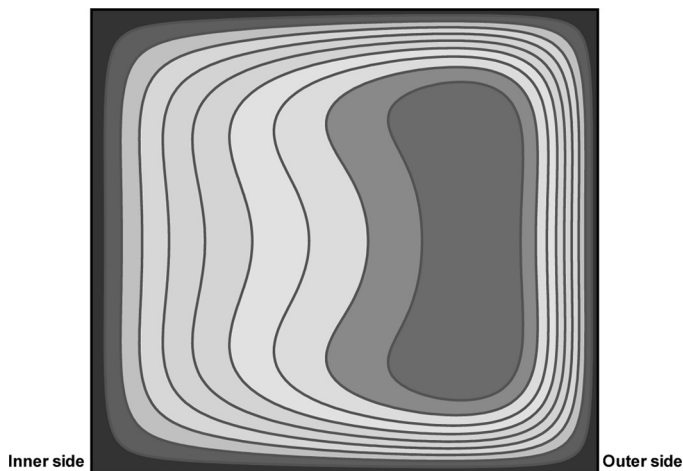
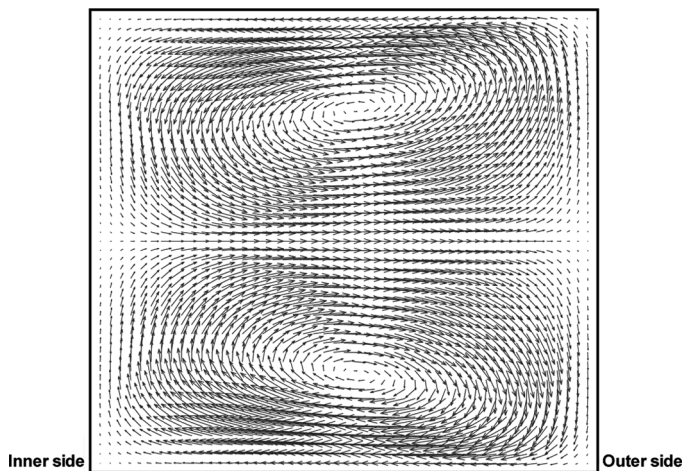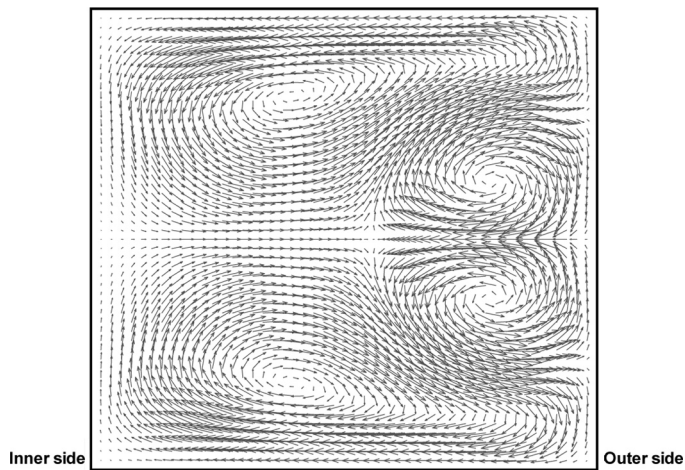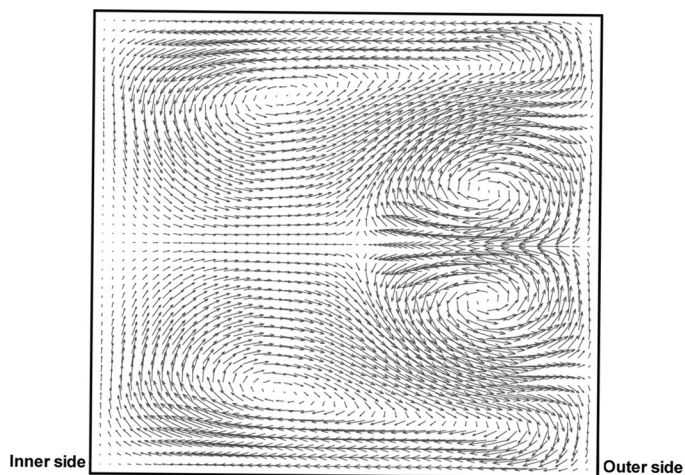**Figure 6.** Velocity contour of cross section (Dn = 100.0, C = 0.05).
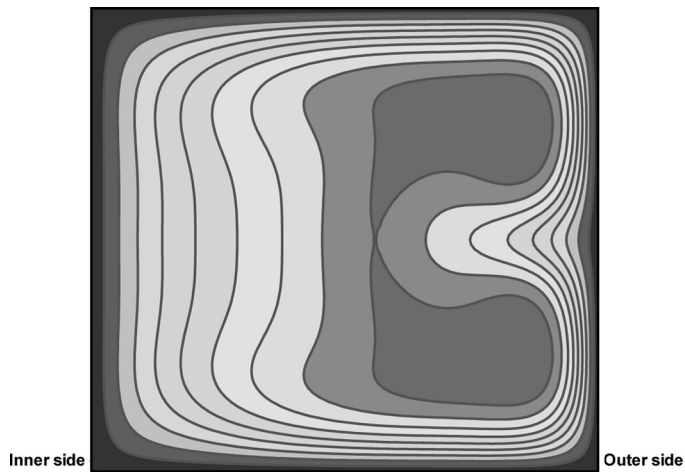
Figure 7. Velocity contour of cross section (Dn=150.0, $C = 0.05$).

Dean number is small, there is just one peak point on the axial velocity profile, and the secondary flow is one pair of weak symmetrical eddies due to the small centrifugal force. As Dean number keeps increasing, the axial maximum velocity moves toward the outside of the wall and, at the same time, the two symmetrical eddies become stronger and stronger, eventually distorting the axial velocity from a single peak to two symmetrical peaks on cross section a–a. On the other hand, once the Dean number exceeds a certain value, the secondary flow suddenly changes from one pair of symmetrical eddies to two pairs of symmetrical eddies
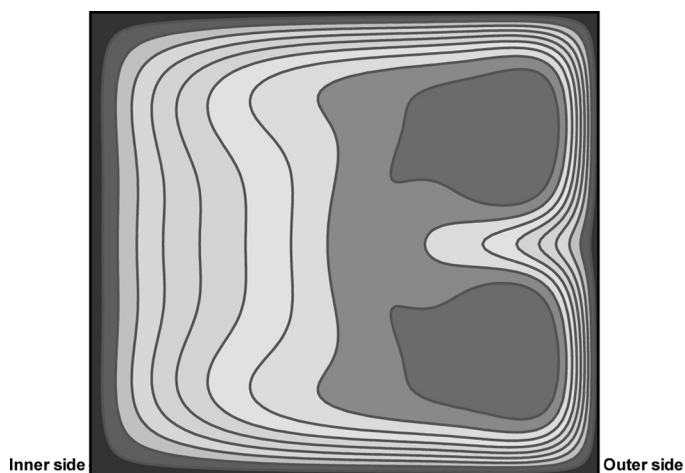
Figure 8. Velocity contour of cross section (Dn $= 200.0$, $C = 0.05$).
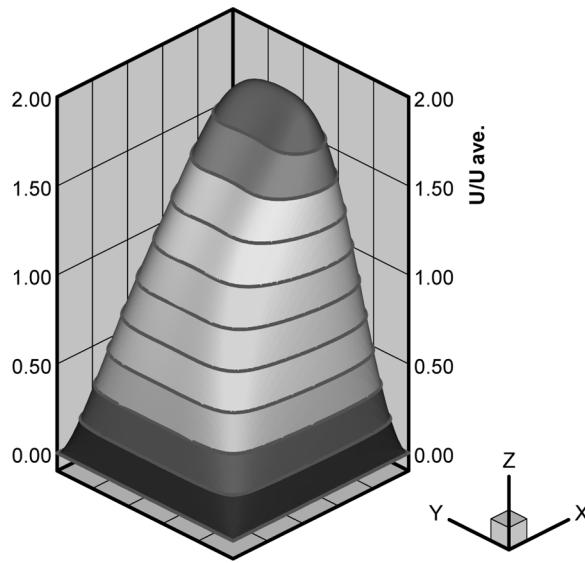
Figure 9. Axial velocity profile in 3-D view (Dn = 50.0, C = 0.05).

(having opposite rotating directions), due to the imbalance between centrifugal force and pressure gradient on the cross section. This is the so-called Dean instability [29, 30]. Therefore, the velocity distribution on section *b–b* suddenly changes
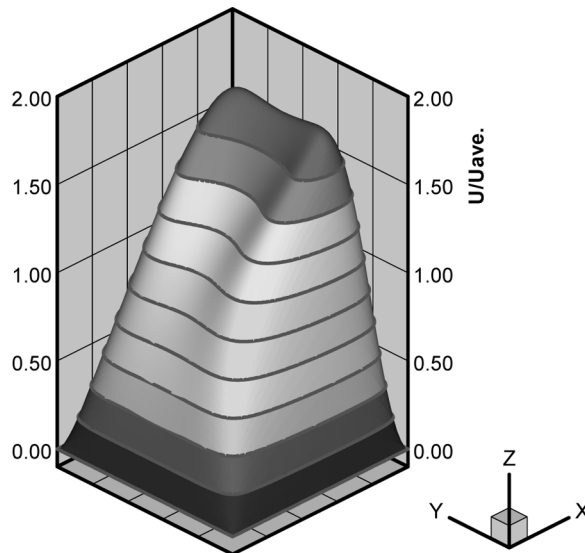
Figure 10. Axial velocity profile in 3-D view (Dn = 100.0, C = 0.05).
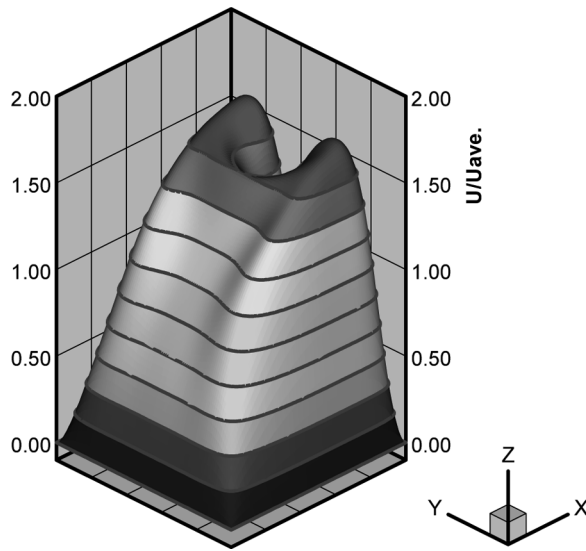
Figure 11. Axial velocity profile in 3-D view (Dn = 150.0, $C = 0.05$).

and another peak velocity appears at cross section a–a, that is, there are now three peak velocities.

In Figures 5–8 and Figures 9–12, the detailed dimensionless axial velocity distributions are presented and the transition process from one velocity peak to two peaks and eventually to three peaks are all clearly shown (i.e., Figures 5–7 or
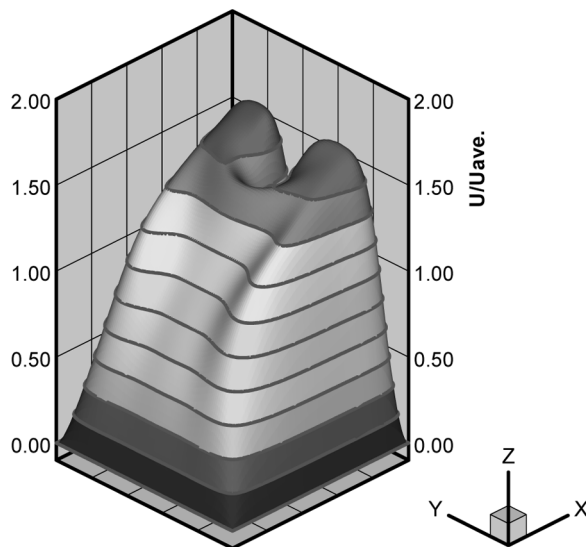
Figure 12. Axial velocity profile in 3-D view (Dn = 200.0, $C = 0.05$).
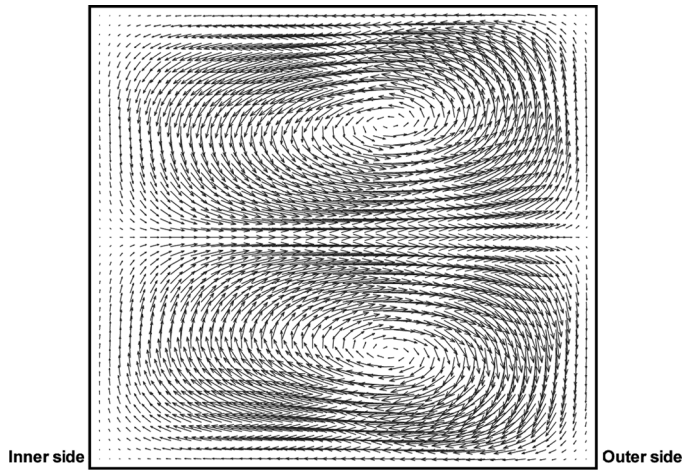
Figure 13. Velocity vector of cross section (Dn = 50.0, C = 0.05).

9–11 in 3-D view). Based on these axial velocity contours, it is obvious that the higher the Dean number, the greater the velocity gradient that will be observed around the duct walls, especially for the two vertical sides, and this is consistent with the previous results in Figure 4. Moreover, since the axial velocity with the same number of uniform contour lines is provided at different Dean numbers, the distribution of uniform contour lines shows how well the axial velocities distribute uniformly on the cross section. From Figures 6–8 or 10–12, one can conclude that the axial velocity trends to be more uniform on the cross-sectional area as the Dean number increases, which is also consistent with Figures 3 and 4.

Figure 14. Velocity vector of cross section (Dn = 100.0, C = 0.05).

Figure 15. Velocity vector of cross section (Dn = 150.0, $C = 0.05$).

In Figures 13–16, the detailed secondary flows on the cross section are presented at different Dean numbers. These figures also clearly show the flow transition from one pair of eddies (in Figures 13 and 14) to two pairs of symmetrical eddies (in Figures 15 and 16) when the Dean number increasing up to certain values. Compared to the single-pair symmetrical eddies, in the double-pair eddies case, the additional pair eddies rotate in the opposite direction on the main vortices (as shown in Figures 15 and 16). The imbalance between the pressure gradient and centrifugal force on the cross section causes the transition from a single-vortex-pair to

**Figure 16.** Velocity vector of cross section (Dn = 200.0, $C = 0.05$).
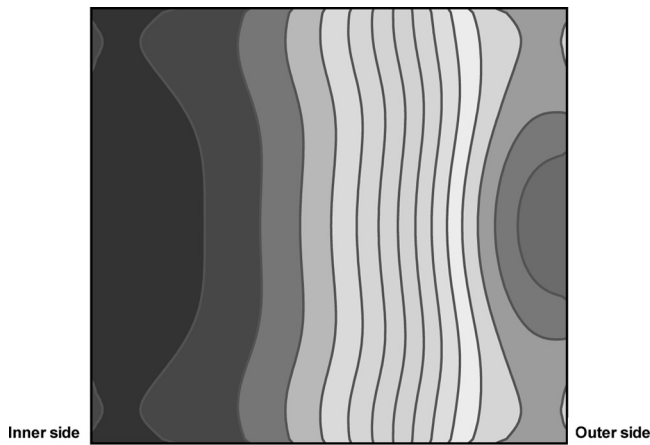
Figure 17. Pressure contour on cross section (Dn = 50.0, C = 0.05).

the double-vortex-pair structure; therefore, the location of maximum axial velocity moves closer to the outer wall in symmetrical positions above and below the radial centerline in Figures 7 and 8 or Figures 11 and 12.

In Figures 17–20 and Figures 21–24, the detailed pressure distributions are presented at different Dean numbers. It is apparent that the pressure contour patterns are considerably different for the double-pair eddies case (in Figures 19 and 20 or Figures 23 and 24) than for the single-pair eddies (in Figures 17 and 18 or Figures 21 and 22). Furthermore, the pressure gradient on the cross section becomes more uniform as the Dean number continues increasing, as shown in Figures 17–19 or Figures 21–23. Since pressure is always a passive variable in fluid
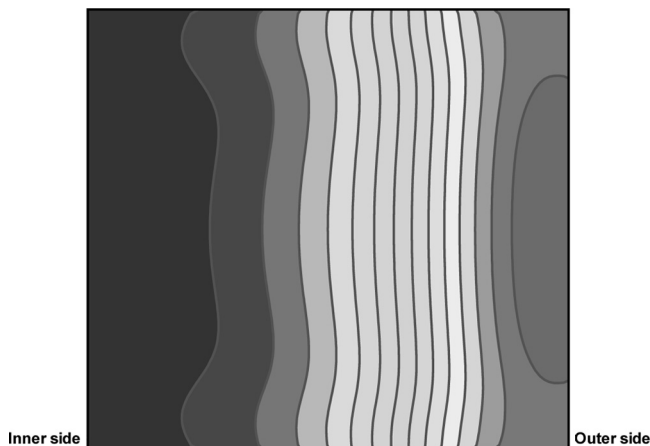

Figure 18. Pressure contour on cross section (Dn = 100.0, C = 0.05).
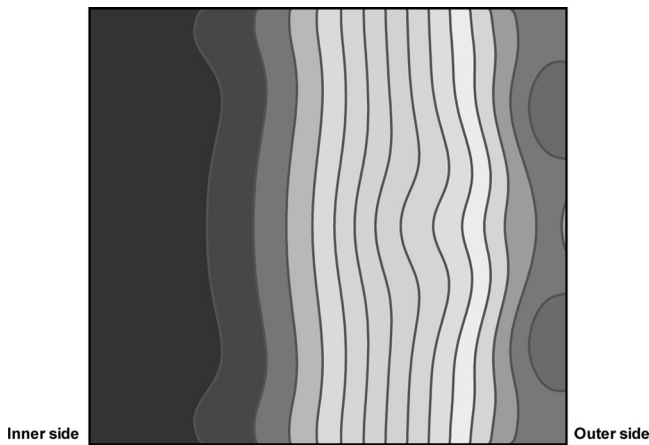
Figure 19. Pressure contour on cross section (Dn = 150.0, C = 0.05).

flow problems, the pressure profiles shown in Figures 17–20 or Figures 21–24 are a consequence of balance between centrifugal force and fluid viscous force.

In real engineering applications, one of the most important results of fully developed flow in curved square duct is estimation of the friction factor (or flow-rate reduction). The available well-known friction factor correlation in the literature [31] is

$$\frac{f_c}{f_s} = 0.225\,\mathrm{Dn}^{0.39} \qquad \text{for a square duct with } 100 < \mathrm{Dn} < 1,500 \qquad (34)$$
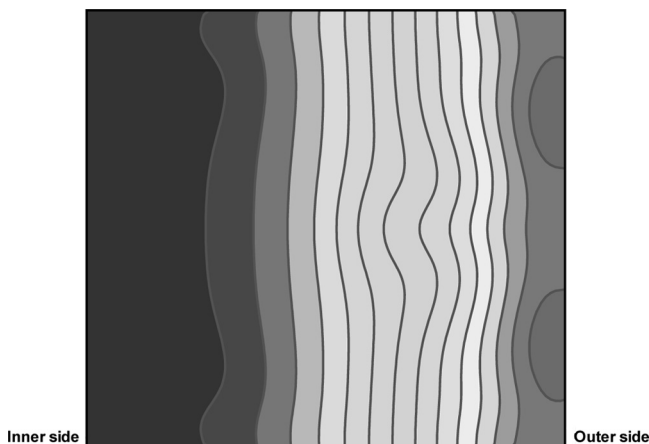
Figure 20. Pressure contour on cross section (Dn = 200.0, C = 0.05).
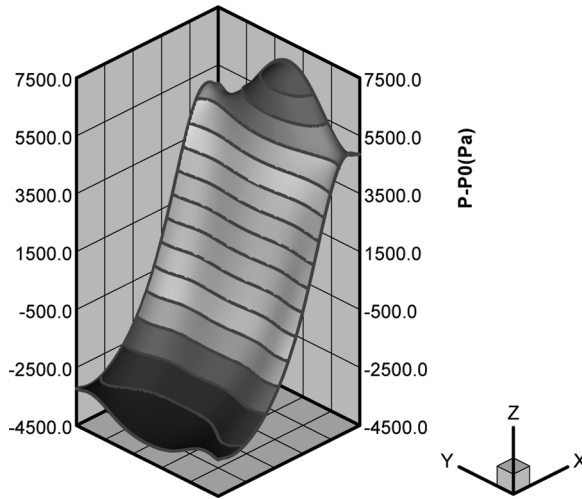
Figure 21. Pressure profile in 3-D view (Dn = 50.0, $C = 0.05$).

In Figure 25, the computed friction factor ratios for a straight square duct at different curvature ratios are presented. It is evident that the presented LBM simulation results are in good agreement with the experimental correlation. On the other hand, it is clearly shown in this figure that the friction coefficient for each specific curvature ratio (from 0.05 to 1.00) changes suddenly when the Dean number is between 115 and 130. This is because when the Dean number increases from 115 to 130, the flow pattern on the cross section changes from one pair of eddies to
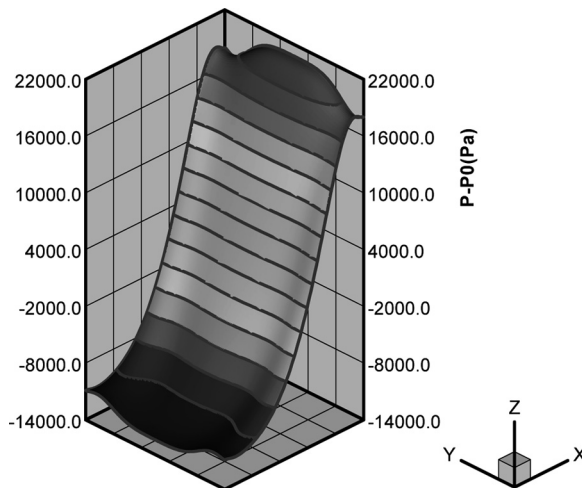
Figure 22. Pressure profile in 3-D view (Dn = 100.0, $C = 0.05$).
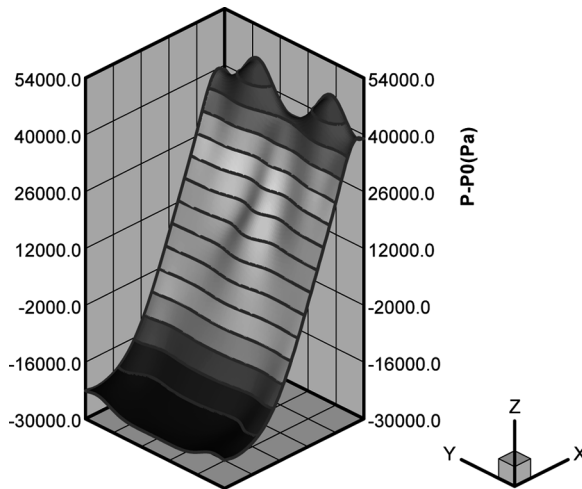
Figure 23. Pressure profile in 3-D view (Dn = 150.0, C = 0.05).

two pair of eddies. This Dean number which identifies the flow pattern is called the critical Dean number. As a consequence of the flow pattern change, the corresponding friction coefficient is increased .

With regard to the transition from single-pair eddies to a double-pair eddies, it was proposed in [32] that, for a curved square duct, the transition is a result of a complex structure of multiple, symmetric, and asymmetric solutions. The singular value of Dean number for the transition of the two- and four-vortex flow patterns
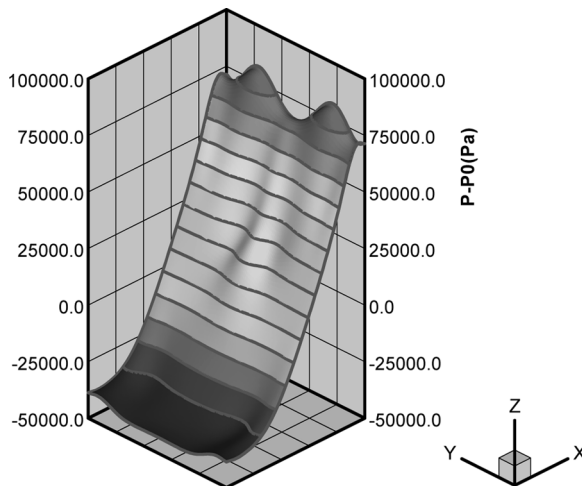
Figure 24. Pressure profile in 3-D view (Dn = 200.0, C = 0.05).
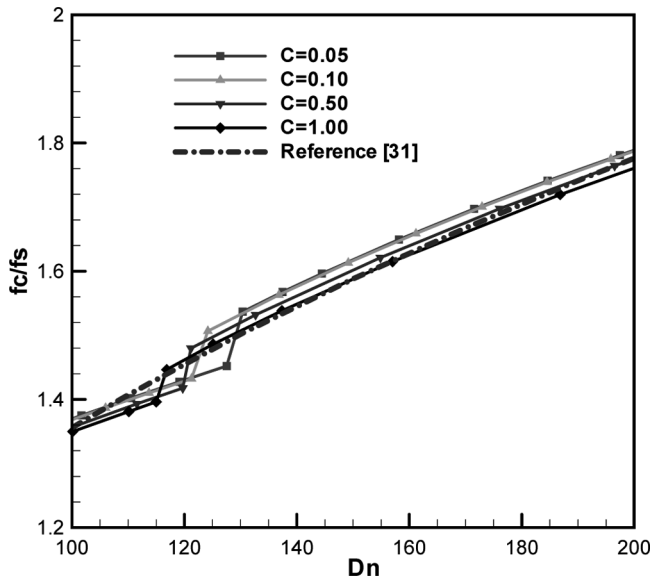
Figure 25. Friction coefficients versus Dean number at different curvature ratios.

is between 113 and 191, which is consistent with the current results obtained from the LBE model, i.e., the critical Dean number is between 115 and 130.

Heat Transfer

In Figures 26–33 and Figures 34–41, the dimensionless temperature contours are presented at different Dean numbers and Prandtl numbers (two kinds of typical
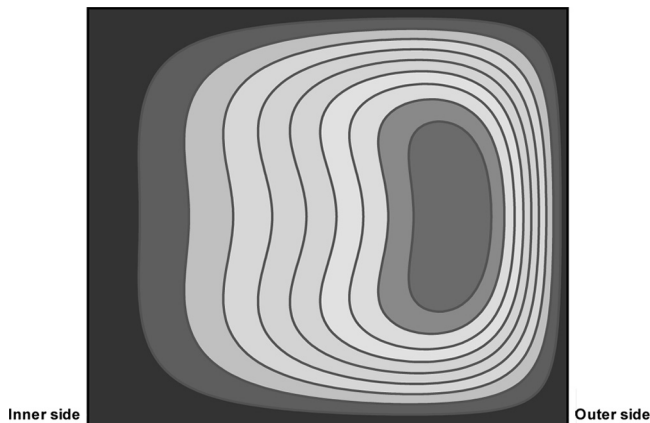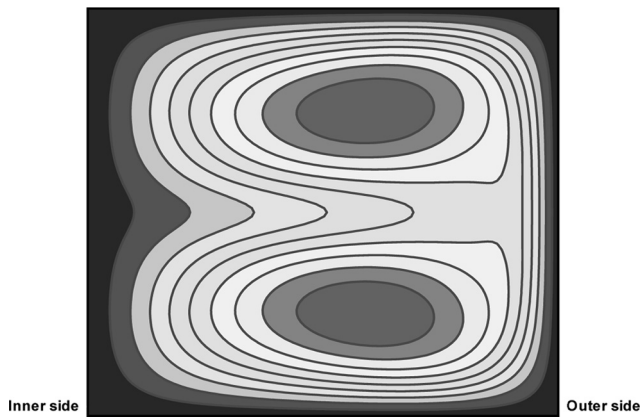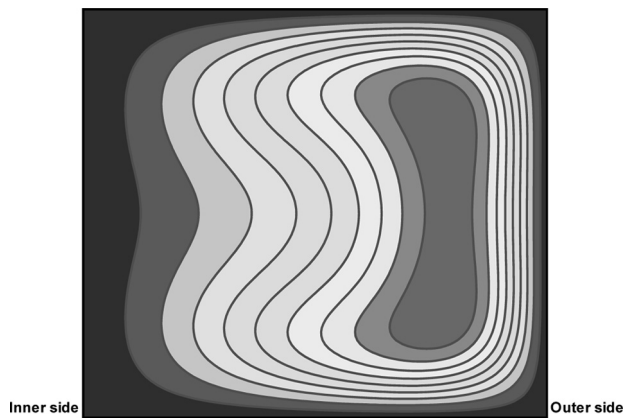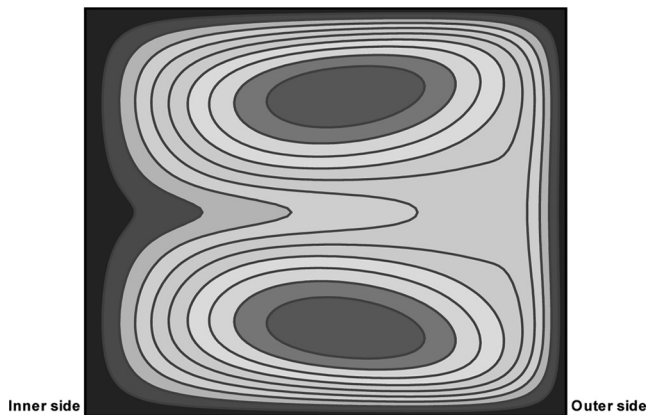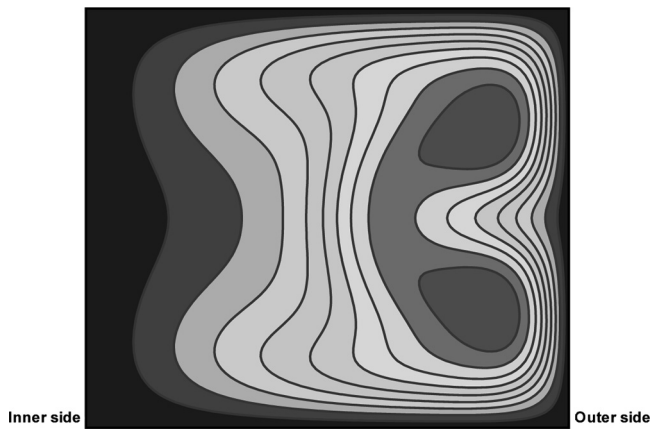

Figure 26. Temperature contour of cross section (Dn = 50.0, Pr = 0.716, $C = 0.05$).

Figure 27. Temperature contour of cross section (Dn = 50.0, Pr = 6.587, C = 0.05).

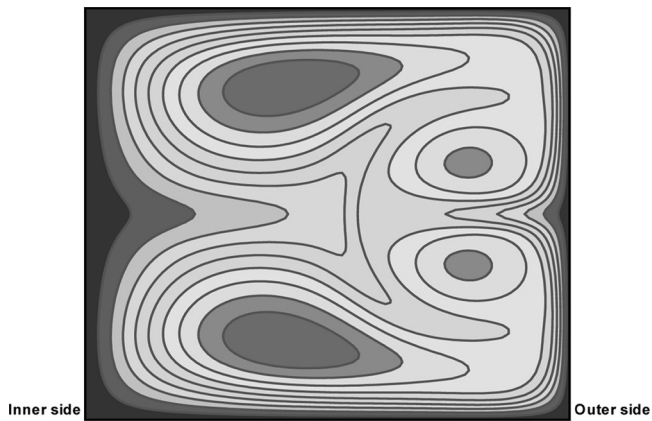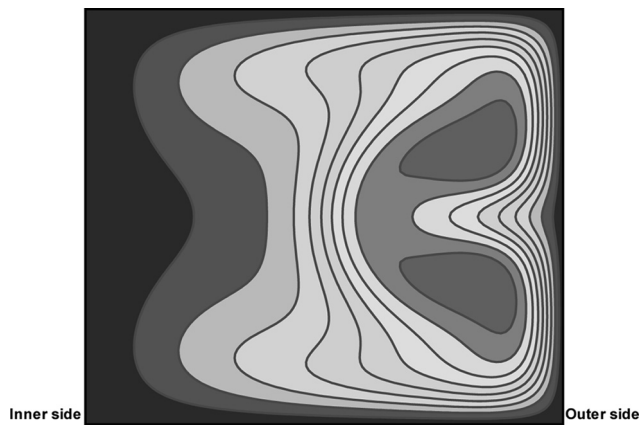**Figure 28.** Temperature contour of cross section (Dn = 100.0, Pr = 0.716, C = 0.05).

Figure 29. Temperature contour of cross section (Dn = 100.0, Pr = 6.587, C = 0.05).

Figure 30. Temperature contour of cross section (Dn = 150.0, Pr = 0.716, C = 0.05).

Figure 31. Temperature contour of cross section (Dn = 150.0, Pr = 6.587, C = 0.05).

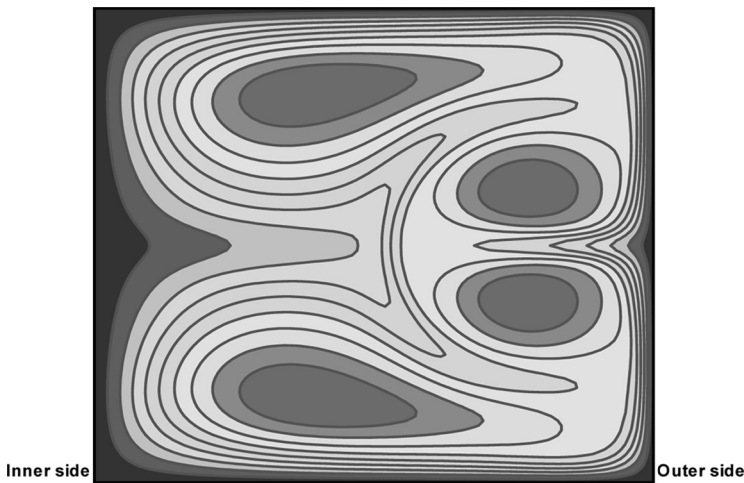**Figure 32.** Temperature contour of cross section (Dn = 200.0, Pr = 0.716, C = 0.05).

Figure 33. Temperature contour of cross section (Dn = 200.0, Pr = 6.587, C = 0.05).

fluid, i.e., air and water, were chosen). From all these figures, it is obvious that the Prandtl number plays a considerable role in the temperature field at a given Dean number and curvature ratio in a curved duct flow. For example, in Figures 26 and 27 or Figures 34 and 35, the fluid flow conditions are exactly the same (i.e., same Dean number and curvature ratio), but the fluid physical properties (i.e., Prandtl number) are different. As a result, the dimensionless temperature contours are significantly different for these two cases with different Prandtl number. Similar results with different Dean numbers are presented in Figures 28–33 or Figures 36–41.
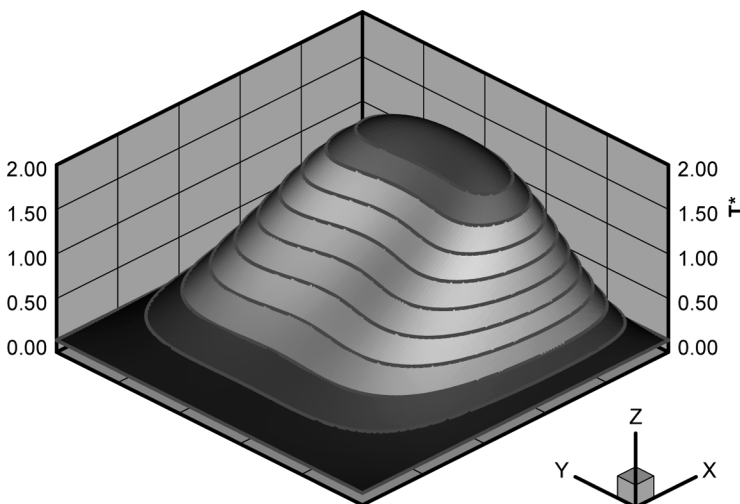

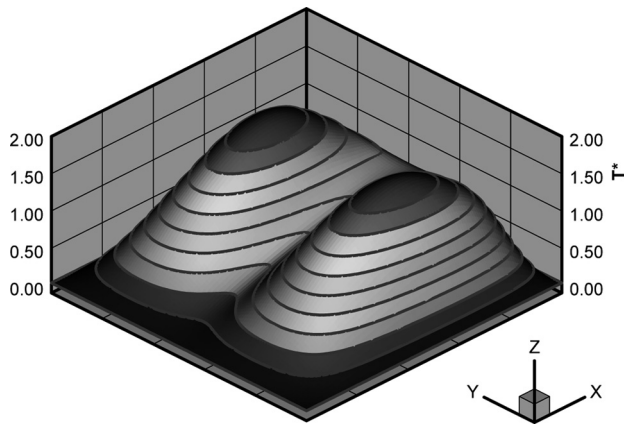**Figure 34.** Temperature profile in 3-D view (Dn = 50.0, Pr = 0.716, C = 0.05).

Figure 35. Temperature profile in 3-D view (Dn = 50.0, Pr = 6.587, C = 0.05).

Figure 36. Temperature profile in 3-D view (Dn = 100.0, Pr = 0.716, C = 0.05).

Figure 37. Temperature profile in 3-D view (Dn = 100.0, Pr = 6.587, C = 0.05).

Figure 38. Temperature profile in 3-D view (Dn = 150.0, Pr = 0.716, C = 0.05).

Figure 39. Temperature profile in 3-D view (Dn = 150.0, Pr = 6.587, C = 0.05).

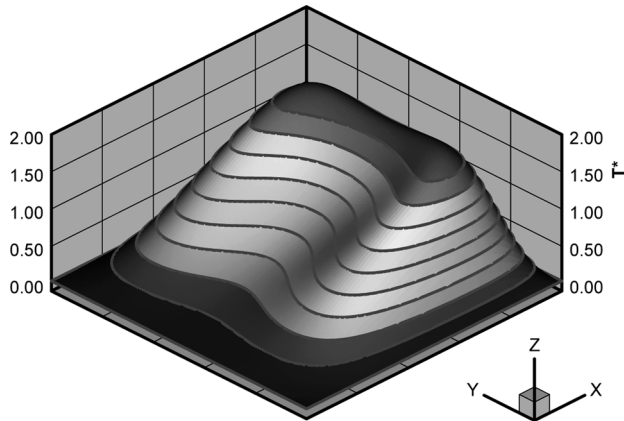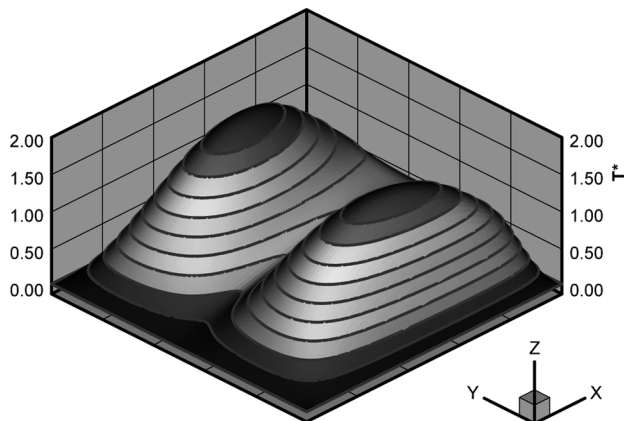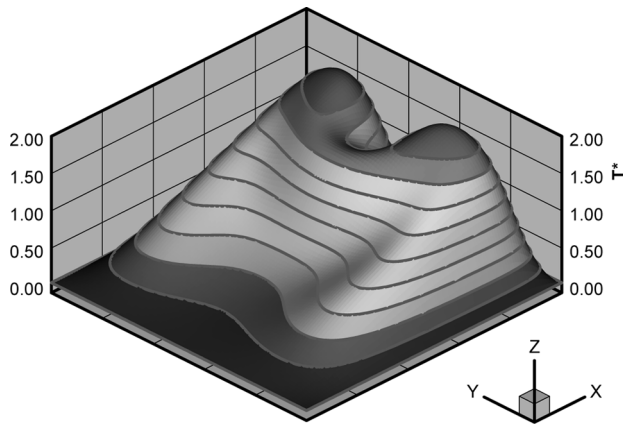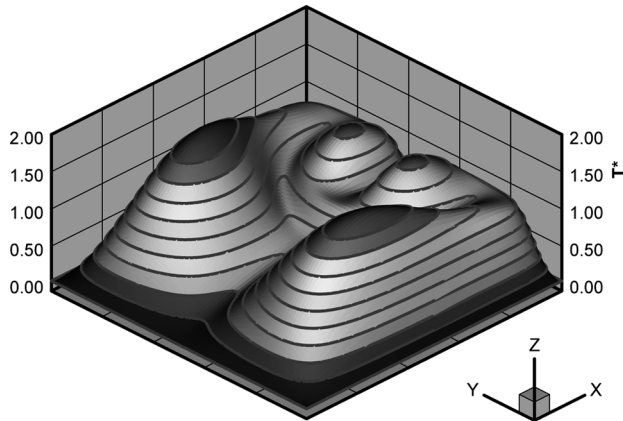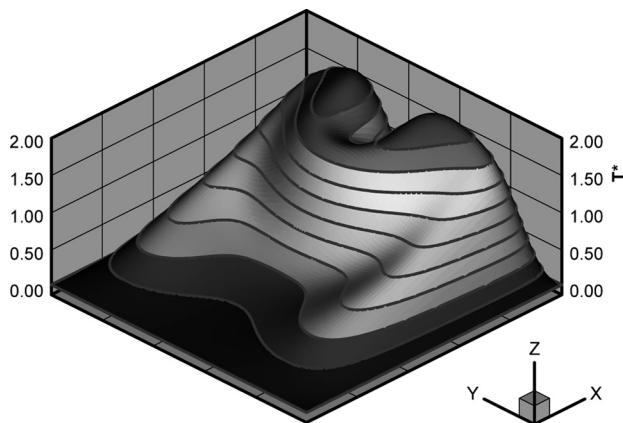**Figure 40.** Temperature profile in 3-D view (Dn = 200.0, Pr = 0.716, C = 0.05).
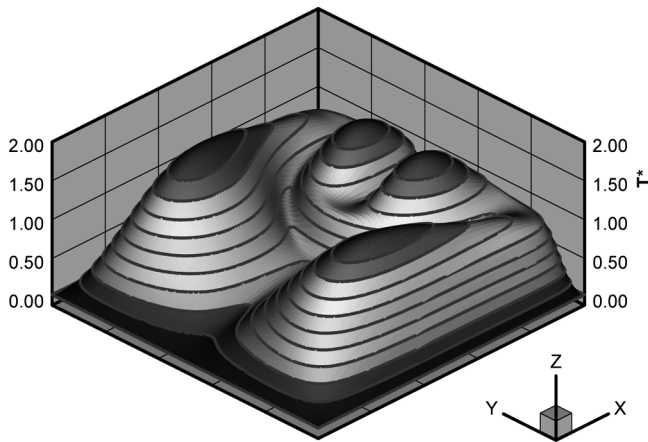
Figure 41. Temperature profile in 3-D view (Dn = 200.0, Pr = 6.587, C = 0.05).
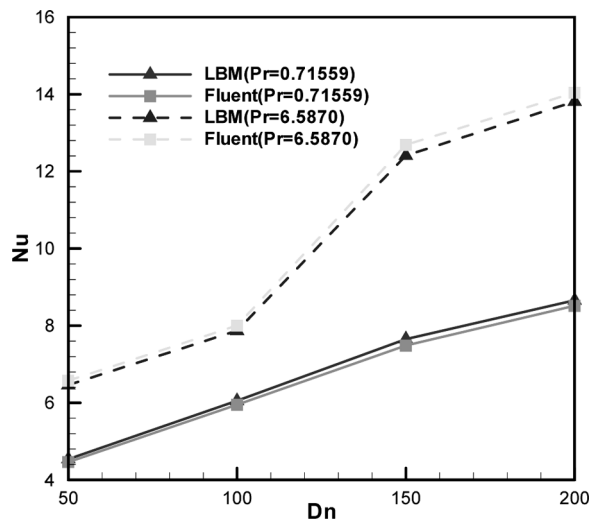
Figure 42. Nusselt number comparisons between LBM and Fluent results (C = 0.05).

Figure 42 shows a comparison of Nusselt numbers between the passive-scalar thermal LBE and Fluent software results with the same fluid flow and heat transfer parameters, including boundary conditions and geometry configurations. Before the thermal results by Fluent software were adopted in Figure 42, the grid convergence test was implemented for fluid flow and heat transfer. It is also apparent from this figure that the results of the LBE are very consistent with those of Fluent software (i.e., the conventional CFD method).

CONCLUSIONS

In this article, the fully developed fluid flow and heat transfer in a square duct with curvature ratio 0.05–1.0 and Dean number 0–200 have been thoroughly investigated using the D3Q27 incompressible LBGK model and the passive-scalar thermal model, respectively. Based on the simulation results, the following conclusions can be drawn.

1. The fluid flow simulation results of the D3Q27 LBE model are in good agreement with experimental correlation at the given conditions.
2. The full Dean stability range as obtained in this article is consistent with results in the literature.
3. The LBE method is a new and useful successive method to solve hydrodynamic problems; compared to the conventional CFD approach, this method is very easy to understand and implement. The unique parallelism characteristics can save a lot of calculation time if a special programming technique is applied.

REFERENCES

1. S. Thangam and N. Hur, Laminar Secondary Flows in Curved Rectangular Ducts, *J. Fluid Mech.*, vol. 217, pp. 421–440, 1990.
2. L. Wang and T. Yang, Bifurcation and Stability of Forced Convection in Curved Ducts of Square Cross-Section, *Int. J. Heat Mass Transfer*, vol. 47, pp. 2971–2987, 2004.
3. C. Herman and E. Kang, Heat Transfer Enhancement in a Grooved Channel with Curved Vanes, *Int. J. Heat Mass Transfer*, vol. 45, pp. 3741–3757, 2002.
4. T. W. Gyves and T. F. Irvine, Jr., Laminar Conjugated Forced Convection Heat Transfer in Curved Rectangular Channels, *Int. J. Heat Mass Transfer*, vol. 43, pp. 3953–3964, 2000.
5. M. D. Su and R. Friedrich, Numerical Simulation of Fully Developed Flow in a Curved Duct of Rectangular Cross-Section, *Int. J. Heat Mass Transfer*, vol. 37, pp. 1257–1268, 1994.
6. D. M. Kirpalani, T. Patel, P. Mehranl, and A. Macchi, Experimental Analysis of the Unit Cell Approach for Two-Phase Flow Dynamics in Curved Flow Channels, *Int. J. Heat Mass Transfer*, vol. 51, pp. 1095–1103, 2008.
7. P. K. Papadopoulos and P. M. Hatzikonstantinou, Numerical Investigation of the Thermally Developing Flow in a Curved Elliptic Duct with Internal Fins, *J. Heat Transfer*, vol. 129, pp. 759–762, 2007.
8. L. Wang and F. Liu, Forced Convection in Slightly Curved Microchannels, *Int. J. Heat and Mass Transfer*, vol. 50, pp. 881–896, 2007.
9. J. Facao and A. C. Oliveria, Modeling Laminar Heat Transfer in a Curved Rectangular Duct with a Computational Fluid Dynamics Code, *Numer. Heat Transfer A*, vol. 48, pp. 165–177, 2005.
10. S. Succi, *The Lattice Boltzmann Equation*, Oxford University Press, Oxford, UK, 2001.
11. S. Chen and G. D. Doolen, Lattice Boltzmann Method for Fluid Flows, *Annu. Rev. Fluid Mech.*, vol. 30, pp. 329–364, 1998.
12. J. Hardy, O. de Pazzis, and Y. Pomeau, Molecular Dynamics of a Classical Lattice Gas: Transport Properties and Time Correlation Functions, *Phys. Rev. A*, vol. 13, pp. 1949–1961, 1976.

13. F. J. Higuera, S. Succi, and R. Benzi, Lattice Gas Dynamics with Enhanced Collisions, *Europhys. Lett.*, vol. 9, pp. 345–349, 1989.
14. U. Frisch, B. Hasslacher, and Y. Pomeau, Lattice-Gas Automata for the Navier-Stokes Equation, *Phys. Rev. Lett.*, vol. 56, pp. 1505–1508, 1986.
15. S. Tajiri, M. Tsutahara, and L. Wu, Improvement of Two-Component Model of the Finite Difference Lattice Boltzmann Method for a Gas-Liquid Flow Simulation, *Proc. 5th Joint ASME/JSME Fluids Engineering Summer Conf.*, FEDSM 2007, pp. 431–436, 2007.
16. K. Iqlberqer, N. Thurey, and U. Rude, Simulation of Moving Particles in 3D with the Lattice Boltzmann Method, *Comput. Math. Appl.*, vol. 55, pp. 1461–1468, 2008.
17. X. He and L.-S. Luo, *Lattice Boltzmann Model for the Incompressible Navier-Stokes Equation*, American Institute of Physics, 1997.
18. Q. Liao and T. C. Jen, Numerical Simulation with Lattice Boltzmann Method (LBM) in the Curved Square Duct, *Proc. 2006 ASME International Mechanical Engineering Congress and Exposition, IMECE2006—Heat Transfer*, 2006.
19. D. A. Wolf-Gladrow, *Lattice-Gas Cellular Automata and Lattice Boltzmann Models*, Springer-Verlag, 2000.
20. X. Shan, Simulation of Rayleigh–Benard Convection Using Lattice Boltzmann Model, *Phys. Rev. E*, vol. 55, pp. 2780–2788, 1997.
21. P. Yuan and L. Schaefer, A Thermal Lattice Boltzmann Two-Phase Flow Model and Its Application to Heat Transfer Problems—Part 1. Theoretical Foundation, *J. Fluids Eng., Trans. ASME*, vol. 128, pp. 142–150, 2006.
22. Y. Peng, C. Shu, and Y. T. Chew, A 3D Incompressible Thermal Lattice Boltzmann Model and Its Application to Simulate Natural Convection in a Cubic Cavity, *J. Comput. Phys.*, vol. 193, pp. 260–274, 2003.
23. J. M. Buick and C. A. Greated, Gravity in a Lattice Boltzmann Model, *Phys. Rev. E*, vol. 61, pp. 5307–5320, 2000.
24. Y. H. Lu and J. M. Zhan, Comparison Between Different Boundary Treatments and Between Different Body Force Term Expressions in Lattice Boltzmann Method, *Zhongshan Daxue Xuebao*, vol. 45, no. 3, pp. 22–26, 2006.
25. Y. A. Cengel and J. M. Cimbala, *Fluid Mechanics Fundamentals and Applications*, McGraw-Hill, New York, 2006.
26. F. P. Incropera and D. P. Dewitt, *Fundamentals of Heat and Mass Transfer*, Wiley, New York, 2001.
27. S. Chen and D. Martinez, On Boundary Conditions in Lattice Boltzmann Methods, *Phys. Fluids*, vol. 8, p. 2527, September 1996.
28. A. D'Orazio and S. Succi, Simulating Two-Dimensional Thermal Channel Flows by Means of a Lattice Boltzmann Method with New Boundary Conditions, *Future Generation Comput. Syst.*, vol. 20, pp. 935–944, 2004.
29. S. Thangam and N. Hur, Laminar Secondary Flows in Curved Rectangular Ducts, *J. Fluid Mech.*, vol. 217, pp. 421–440, 1990.
30. G. J. Hwang and C.-H. Chao, Forced Laminar Convection in a Curved Isothermal Square Duct, *J. Heat Transfer*, vol. 113, pp. 48–53, February 1991.
31. K. C. Cheng and M. Akiyama, Laminar Forced Convection Heat Transfer in Curved Rectangular Channels, *Int. J. Heat Mass Transfer*, vol. 13, pp. 471–490, 1970.
32. K. H. Winter, A Bifurcation Study of Laminar Flow in a Curved Tube of Rectangular Cross-Section, *J. Fluid Mech.*, vol. 180, pp. 343–369, 1987.